Exchange explosions of topological edge defects in a square micromagnet

Sam D. Slöetjes, Erik Folven, and Jostein K. Grepstad

Department of Electronic Systems, NTNU, NO-7491, Trondheim, Norway

The magnetodynamic properties of a square thin-film micromagnet (2 μm × 2 μm × 16 nm) with a flux-closure magnetic ground state were investigated by micromagnetic simulations. The system was excited with an applied magnetic field, displacing the vortex core sufficiently far from its equilibrium position to result in a nonlinear relaxation upon removal of the field. We find that creation of edge topological defects leads to exchange explosions and periodic emission of short-wavelength spin waves emanating from these defects. The exchange explosions of the edge topological defects are investigated and explained in terms of vortex/antivortex creation and the formation of a Bloch point. This finding could prove useful to the development of nanoscale devices for periodic generation of high-frequency microwave radiation.

I. INTRODUCTION

Magnetic vortex core dynamics in two-dimensional ferromagnetic systems have been extensively studied over the past decade [1–3] and continue to fascinate the magnetics community [4,5]. Recently, using vortex cores for manipulation of qubits–the building blocks of quantum computers–has been investigated [6]. The large gradient in the out-of-plane stray field at the vortex core permits addressing individual spins only nanometers apart, in a spin register [7]. So far, investigations of the behavior of magnetic vortices were primarily focused on the dynamics associated with switching the polarity of the vortex core. This switching process involves a so-called "exchange explosion" initiated by the nucleation of a Bloch point [8,9], after which spin waves are emitted. In this work, we use the micromagnetic simulation package MUMAX3 [10] to investigate the dynamic behavior of topological edge defects, which are seen to perform similar exchange explosions. As our model system, we use a square 2 μm × 2 μm × 16 nm La$_{0.7}$Sr$_{0.3}$MnO$_3$ (LSMO) thin-film micromagnet with magnetocrystalline easy axes oriented along the square edges. In this system, the ground-state magnetization is a Landau flux closure, cf. Fig. 1(a). We have previously demonstrated [11] that excitation with an external magnetic field oriented at 45° with the edges leads to a vortex core displacement along the square diagonal [Fig. 1(b)], followed by creation of edge topological defects with a fractional winding number [12] upon increasing the applied field, cf. Fig. 1(c). Such edge topological defects were previously investigated by van den Berg *et al.* [13,14], where the defects were referred to as "wall clusters." In their papers, the authors recognize the significance of these critical spin textures for tracking the magnetization during changes in the domain structure of patterned thin-film magnets. In our case, the creation of edge topological defects leads to a domain state also known as the "tulip pattern" [15,16]. The controlled creation of edge topological defects renders this model system a suitable platform to study the dynamics of such defects.

II. DYNAMICS OF THE EDGE DEFECTS

The micromagnetic parameters used for LSMO in the present simulations were an exchange stiffness constant $A_{ex} = 1.7$ pJ/m, a saturation magnetization $M_S = 400$ kA/m, and a biaxial anisotropy constant of $K_1 = 1.6$ kJ/m^3 [17–19]. The Gilbert damping was set to $\alpha = 0.01$. The in-plane cell size was $l_x \times l_y \times l_z \approx 2 \times 2 \times 2$ nm^3, which is well below the magnetostatic exchange length, defined as $l_S = \sqrt{2A_{ex}/(\mu_0 M_s^2)} = 4.11$ nm, and appropriate for simulation of Bloch point dynamics, an important factor in vortex core dynamics. The thickness of the square platelet was set to $t = 16$ nm, corresponding to 8 simulation cells in the z direction, and the magnetization was recorded every 2.5 ps.

Starting from the tulip state with fractional defects on the edges of the square micromagnet, the vortex core exhibits an irregular wobbling motion towards the equilibrium position upon removal of the applied field, before the onset of gyration (not shown here). From Fig. 2(a), it can be seen that whenever the vortex core changes direction in this wobbling motion, it also changes polarization p. This behavior is brought about by the gyroforce, $\mathbf{F} = -\mathbf{G} \times \mathbf{v}$, which also accounts for the gyrotropic motion of the vortex core [1,20] and originates from the Thiele equation [20,21]:

$$-\mathbf{G} \times \frac{d\mathbf{X}}{dt} - \hat{\mathbf{D}}\frac{d\mathbf{X}}{dt} + \frac{\partial W(\mathbf{X})}{\partial \mathbf{X}} = 0,$$

In this equation, $\mathbf{X} = (X, Y)$ is the position of the vortex core, $\hat{\mathbf{D}}$ is the damping tensor, W is the potential energy of the vortex, and $\mathbf{G}$ is the "gyrovector." The latter determines the direction of motion and is given by $\mathbf{G} = -\frac{2\pi}{\gamma}npt\mu_0 M_s\hat{\mathbf{z}}$, where $\hat{\mathbf{z}}$ denotes the out-of-plane unit vector. Here, γ is the gyromagnetic ratio, M_s the saturation magnetization, and t the sample thickness. The polarization p is the out-of-plane direction of the vortex core ($p = +1$ for up, $p = -1$ for down), and n is the topological winding number which is $n = +1$ for a vortex and $n = -1$ for an antivortex.
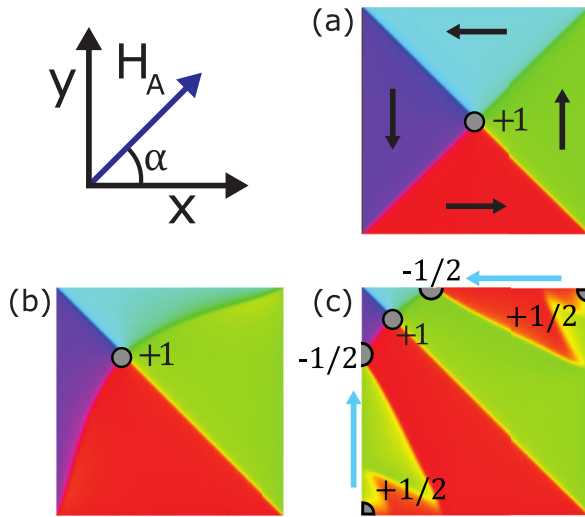
FIG. 1. Magnetic domain-state transition upon application of an external field at an angle of 45° with the square edges; (a) ground-state magnetization in the absence of an applied field, featuring a vortex topological defect with winding number $n = +1$ at the center, (b) displacement of the vortex core in a magnetic field, and (c) creation of edge topological defects with fractional winding numbers upon increasing the applied field.

Henceforth, we focus on the dynamics of the edge topological defects in our square micromagnet. In the static case, the fractional edge topological defects have no out-of-plane magnetization. Hence the gyrovector **G** is zero, and little interesting dynamic behavior can be expected upon removal of the field. Since the magnetic moments which constitute the edge topological defects rotate 180° (from the $+y$ to $-y$ direction) over a distance of approximately 50 nm, the exchange energy associated with such defects is small compared to that of a vortex ($n = +1$)/antivortex ($n = -1$) core. However, when the edge topological defects obtain a velocity, an effective "gyrofield" will act on the spins within the defect [2,22]. The gyrofield $\boldsymbol{H}_G \propto 1/\gamma (\mathbf{m} \times \dot{\mathbf{m}}) = -1/\gamma (\mathbf{m} \times (\mathbf{v} \cdot \nabla)\mathbf{m})$, where **v** is the velocity of the defect. Since all the spins in the defect are at the outset lying in the plane, $\boldsymbol{H}_G$ will be oriented in the out-of-plane direction. At large enough velocities ($\sim$100 m/s), the gyrofield is sufficiently strong ($\sim$0.2 T) to provide the edge defect with an out-of-plane component, which also leads to a contraction of the defect [cf. Fig. 3(b)].

The edge topological defects are seen to repeatedly perform exchange explosions followed by emission of spin waves, as indicated on the left edge of the square in Fig. 2(a) (Supplemental Video 1 [23]). In the upper panel of Fig. 2(b), the position of this edge topological defect is plotted versus time, reflecting the repetitive pattern of edge defect propagation. The time interval between exchange explosions is seen to decrease as the edge defect progresses along the edge. The propagation velocity drops to zero for every exchange explosion [cf. lower panel of Fig. 2(b)] and peaks at approximately $v \approx 100 \pm 5$ m/s in between these events. In the following, we focus on events in the time interval $2.5-5$ ns after removal of the field, i.e., the second exchange explosion in Fig. 2.
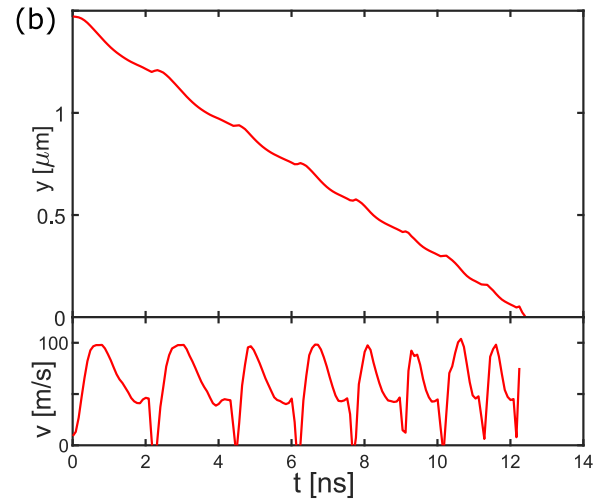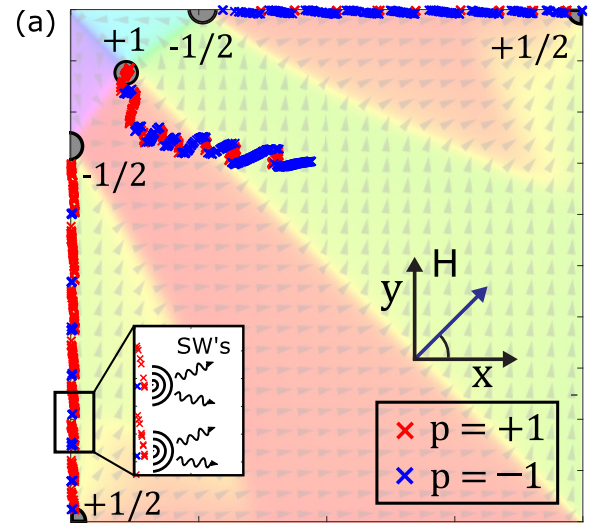

FIG. 2. (a) The motion of topological defects following removal of the applied field, after the creation of edge topological defects. The red/blue markers indicate the defect positions, and their color indicates the polarization direction. (b) Upper panel: position of the edge topological defect versus time; lower panel: velocity of the edge topological defect versus time.

In Fig. 3(c), the evolution of the m_x, m_z components of the magnetic moment at the $n = -1/2$ edge defect core (left edge) vs time is illustrated for two exchange explosions. The initial magnetization is shown with positive m_x and m_z components, followed by precession in the x,z plane as time progresses. This precession continues until the exchange explosion takes place, and the magnetization reverts abruptly to the initial configuration.

The spatial profile of the spin wave emitted by the defect during an exchange explosion is displayed in the upper graph of Fig. 3(d). The profile $m_z(y)$ is recorded for moments along the edge of the square in the immediate vicinity of the defect and shows that the maximum out-of-plane component of the spin wave is $\sim$5% of the saturation magnetization. In order to assess the wavelength of this spin wave, the corresponding power spectrum is found by Fourier transformation of this
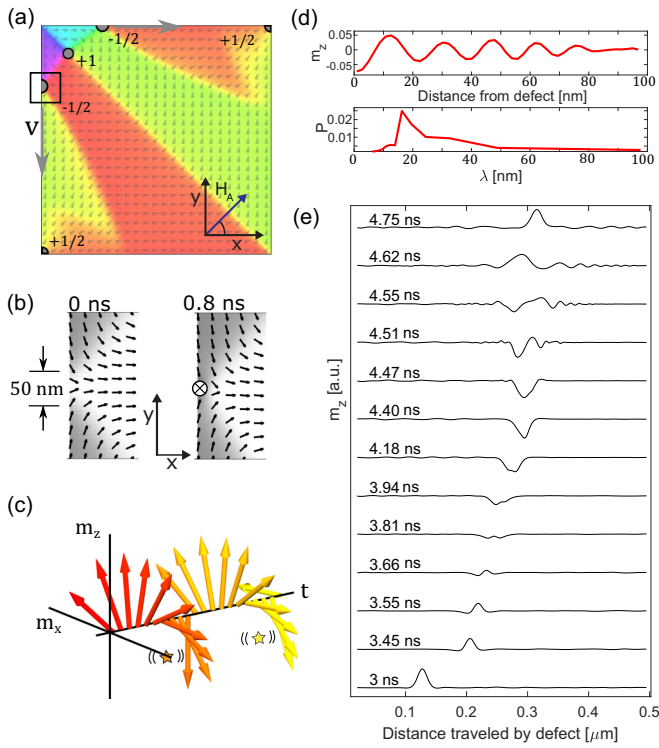
FIG. 3. Motion of the edge topological defects; (a) the edge defect under consideration encircled with a black square. Traveling down the edge, this defect intermittently emits bursts of spin waves; (b) zoom-in on the region marked (black square) in (a) 0.8 ns after removal of the external field; (c) in-plane (m_x) and out-of-plane (m_z) components of the magnetization at the core of the edge defect as a function of elapsed time. The magnetization is averaged over the film thickness, and arrows indicate the direction of the averaged moments. The exchange explosions are indicated by the star; (d) upper graph: out-of-plane magnetization of the spin wave emitted after an exchange explosion of the edge defect, lower graph: power spectrum of the spin wave with maximum power at a $\lambda = 16$ nm. (e) z component of the magnetization, averaged over the film thickness and plotted against position measured along the y axis vs elapsed time after field removal, showing the exchange explosion at 4.5 ns. All timestamps correspond to elapsed time after field removal.

$m_z(y)$ profile and is shown in the lower graph of Fig. 3(d), indicating a wavelength of $\lambda \approx 16$ nm.

In Fig. 3(e), the out-of-plane component m_z at the edge defect, averaged over the cells in the z direction, is plotted versus time for a section of the left-hand edge of the micromagnet. At $t = 3$ ns, the defect has a positive out-of-plane magnetization $m_z = M_s$, corresponding to $p = +1$. After $t = 3.45$ ns, the z component of the defect magnetization is attenuated to $m_z \approx M_s/2$ and continues to decrease until $t = 3.8$ ns, when the x component has grown to $m_x \approx -M_s$, with $m_z \approx 0$. At $t = 4.4$ ns, m_z has attained a local minimum of $m_z \approx -0.95\,M_s$ (corresponding to $p = -1$), which can also be observed in Fig. 2(b) as the blue markers along the left-hand edge of the square. Figure 3(c) shows the concurrent increase in m_x with the reduction of m_z.

At $t = 4.5$ ns, the exchange explosion is triggered, and appears as a sudden outburst in out-of-plane magnetization followed by emission of short-wavelength spin waves. These spin waves emanate radially from the edge defect, and can be seen to travel in the $\pm y$ directions [cf. Fig. 3(e)] with a wavelength of approximately $\lambda = 16$ nm. The phase velocity of these spin waves was calculated at $v = 355$ m/s. While the polarization of a topological defect with winding number $n = +1$ changes polarization after an exchange explosion, the polarization of this edge defect invariably reverts to its initial value $p = +1$ after an explosion. Following the exchange explosion at $t = 4.5$ ns, the local peak in m_z is restored, and the process occurs repeatedly 8 times as the $n = -1/2$ defect moves down the left-hand edge of the square micromagnet. The inverse behavior in terms of polarization ($p = +1 \rightarrow p = -1$) can be observed for the edge topological defect traveling along the top edge of the square.

III. ANALYSIS OF THE EXCHANGE EXPOSIONS

In order to gain a better understanding of the mechanism driving the exchange explosions of the traveling $n = -1/2$ edge topological defect, we zoom in on a region of lateral extension 25 nm × 25 nm surrounding this defect. Figure 4 shows plots of the in-plane spin configuration in the immediate vicinity of the defect in the thin-film micromagnet. We find, as the $n = -1/2$ defect travels down the edge, that an antivortex (AV) with positive polarization ($p = +1$) is nucleated and expelled into the square. After 3.1 ns, this AV has traveled 15 nm into the interior of the structure. As a result of the AV expulsion, the edge defect transforms into an $n = +1/2$ defect in order to preserve the total winding number of this defect and the AV combined. At 4.375 ns, a vortex (V) with negative polarization ($p = -1$) is nucleated at the fractional defect, and the edge defect returns to its initial state with winding number $n = -1/2$. The vortex is fully separated from the edge defect at $t = 4.425$ ns and travels towards the AV. The V-AV pair annihilates at $t = 4.45$ ns, leaving behind the $n = -1/2$ defect only. This V-AV annihilation triggers the exchange explosion.

The expulsion of the AV and V and the concurrent transformation of the edge defect have been observed before in the context of Walker breakdown for domain-wall (DW) motion in thin ferromagnetic strips [24]. Walker breakdown denotes the periodic deformation of a head-to-head or tail-to-tail DW in a one-dimensional (1D) ferromagnetic wire or a thin ferromagnetic strip [25] and appears as a precession of the DW spins around the wire axis, while continuously generating spin waves that travel outward from the DW center [26]. Through this mechanism, an upper bound is imposed on the DW velocity. In our case, the edge topological defect is linked to a head-to-head DW between spins along the edge of the square, and the DW precession is seen in Fig. 3(c). However, the spin waves are created in "bursts" and not continuously. The difference can be explained by the fact that our system is not 1D, and continuous generation of spin waves is impeded by exchange coupling to the moments surrounding the edge defect. The situation is comparable to a strip with a small but finite width, where a DW consists of two oppositely charged topological edge defects on each side of the strip [12]. In such strips, Walker breakdown occurs through intermittent exchange of Vs/AVs between the two edge defects, as the DW reaches a certain critical velocity [24,27–29]. In the present case, there is no oppositely charged defect to "absorb" the
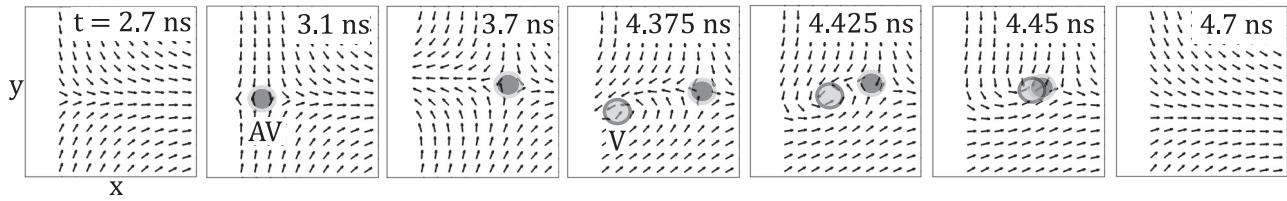
FIG. 4. Vortex (V) and antivortex (AV) motion in a 25 nm × 25 nm area on the edge of the square micromagnet. Every arrow occupies a surface of 2 nm × 2 nm.

(A)V in our square micromagnet model system, and the edge defect thus builds up exchange energy which leads to an exchange explosion.

The annihilation of a V-AV pair with opposite polarization is known to involve the creation and subsequent annihilation of a Bloch point (BP), which moves through the full thickness of the thin-film magnetic structure [8]. A BP is a spherical object in the three-dimensional magnetization texture, and is characterized by zero magnetization at its center. As such, the most straightforward way to find the coordinates of a BP is by determining the intersection of the $m_x = 0$, $m_y = 0$, and $m_z = 0$ isosurfaces. A BP has a nonvanishing skyrmion number which can be calculated by integrating the magnetization over a surface containing the BP [30]. We adopt a slightly modified version of the method used in Ref. [8] in order to represent graphically the Bloch point dynamics during the V-AV annihilation process, as shown in Figs. 5(a)–5(i) (Supplemental Video 2 [23]). To this end, we represent the V/AV structure by isosurfaces of $m_z/M_s = +0.7$ (maroon, representing the AV) and $m_z/M_s = -0.7$ (blue, representing the V). The BP is shown as a black sphere. The color code represents the value of m_z at the thin film bottom surface, and the timestamp indicates the elapsed time since the nucleation of the vortex ($t = 4.375$ ns, cf. Fig 4), in order to avoid cumbersome

notation. The simulation area in the (x,y) plane is the same as that in Fig. 4, so that the edge of the square micromagnet coincides with the left edge in Fig. 5, and the z direction extends throughout the entire film thickness, i.e., 16 nm.

Figure 5(b) shows that the V/AV annihilation is initiated at $t = 75$ ps, at the (x,y) position where the separation between blue and maroon isosurfaces is at a minimum. The BP then emerges from the bottom surface of the thin-film micromagnet and moves upward through the film. Concurrently, the AV (maroon) and V (blue) are seen to retreat from the bottom surface, traveling upward with the BP. However, as the spins with $m_z > +0.7$ nearly vanish by the end of the annihilation process [cf. Fig. 5(i)], the spins with $m_z > -0.7$ still extend throughout the entire film thickness. In approximately 40 ps, the BP has moved through the full thickness of the square platelet, indicating a vertical speed of $v_{BP} \approx 400$ m/s. Figure 5(j) indicates that the BP follows an oscillatory trajectory in the (x,z) plane, as it travels through the film. A lateral swing of approximately 1.5 nm suggests that this erratic motion may be related to the mesh discretization of 2 nm in the x direction, as a similar phenomenon was observed in Ref. [30].

The defect on the upper edge of the square micromagnet [cf. Fig. 3(a)] also exhibits exchange explosions. We found
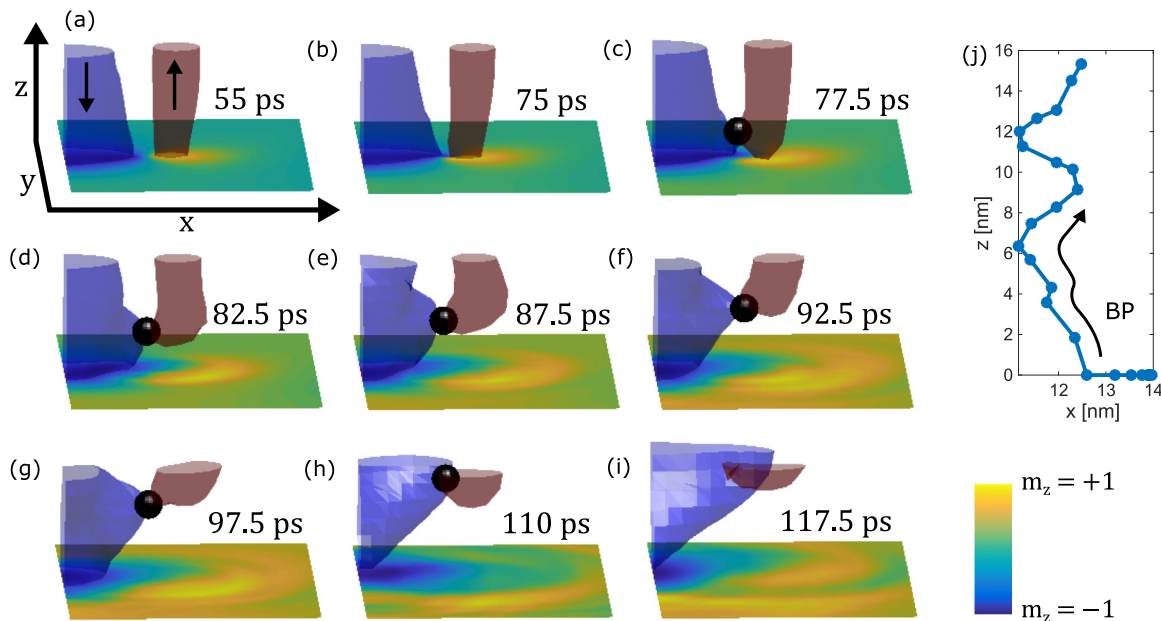

FIG. 5. (a)–(i) Motion of the Bloch point (depicted as a black dot) during an exchange explosion. Timestamps are defined similarly to those in Fig. 4. The blue and maroon surfaces are isosurfaces of $m_z/M_s = -0.7$ and $+0.7$, respectively. (j) Projected motion of the BP onto the (x, z) plane, showing a wobbling motion as the BP travels from the bottom towards the top surface of the film.
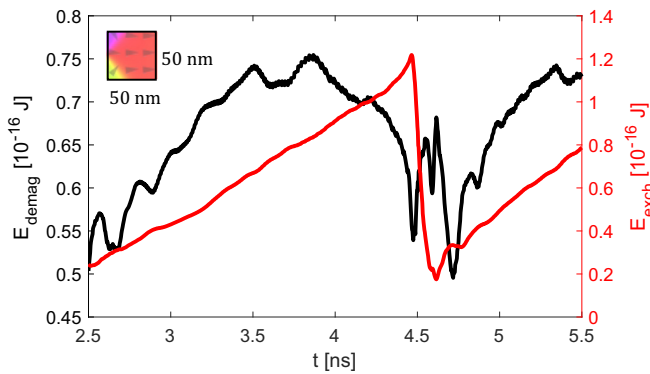
FIG. 6. Demagnetization (black) and exchange energy (red) versus time elapsed after removing the field, reflecting an exchange explosion at $t = 4.5$ ns. The inset depicts the region over which the energy densities were integrated.

the process of V/AV formation and subsequent BP generation to mirror that of the $n = -1/2$ defect on the left edge of the square. The only difference is that the polarization of the V/AV pair is opposite, i.e., the AV has $p = -1$, and V has $p = +1$. This can be explained by an opposite sign of the gyrofield responsible for the out-of-plane magnetization formation [22], as introduced above. The defects on the left and upper edges of the square travel in opposite directions, which gives a sign difference in v, and thus a sign difference in H_G^z.

Demagnetization and exchange energies constitute the two leading-energy terms involved in these exchange explosions. We have assessed these energies by integrating the demagnetization and exchange-energy densities over a 50 nm × 50 nm region, corresponding to the open square surrounding the $n = -1/2$ defect in Fig. 3(a). In Fig. 6, these energies are plotted against elapsed time following removal of the applied field. The energy densities were computed every 2.5 ps, starting after the first exchange explosion. As time progresses, up to 4.5 ns, the defect exchange energy increases almost linearly from $E_{exch} = 0.2 \times 10^{-16}$ J to 1.2×10^{-16} J. At this point, another exchange explosion takes place, and the exchange energy drops significantly. This observation implies that the edge defect builds up exchange energy as it travels down the edge, and this energy is subsequently released by emission of spin waves in the exchange explosion.

The demagnetization energy follows a more irregular trajectory, but can be seen to increase from $t = 2.5$ to 3.8 ns,

where it peaks at $E_{dem} = 0.75 \times 10^{-16}$ J, followed by a sharp drop close to $t = 4.5$ ns. The time dependence of the demagnetization energy was compared to the AV/V nucleation process. It was found that the increase in demagnetization energy can be associated with the emerging (positive) out-of-plane magnetization at the edge defect. Specifically, we note that the expulsion of the AV coincides with the culmination of E_{demag}. The subsequent decrease in demagnetization energy coincides with the development of the vortex with opposite polarization. The demagnetizing energy is reduced due to cancellation of the stray fields produced by the oppositely polarized V and AV. In order to check for the dependence of the V/AV formation on the local demagnetizing field, we also performed simulations of ultrathin micromagnets (layer thickness of 2 nm). For these thinner platelets, we find that the development of an out-of-plane magnetization component is suppressed by the increased local demagnetizing field. This inhibits the V/AV formation at the edge defect, and no exchange explosions are observed.

IV. CONCLUSION

We have investigated the dynamic demagnetization process for a square micromagnet following excitation with an external magnetic field. We find that the edge topological defects nucleated in the transition from a flux closure to a Z-shaped (or tulip) domain pattern undergo periodic exchange explosions when traveling along the edge of the magnet. These repetitive exchange explosions are found to originate from the annihilation of a V/AV pair with opposite polarization. These spin structures are expelled by the edge defect and are localized near ($\sim$15 nm) the edge of the square micromagnet. The annihilation process involves a Bloch point and results in the emission of spin waves with a wavelength of $\lambda = 16$ nm, propagating outward from the defect. The present analysis effectively describes a device that converts Zeeman energy to localized short-wavelength spin waves in a periodic manner, which may prove useful to the development of nanoscale high-frequency microwave radiation devices.

[1] B. Van Waeyenberge, A. Puzic, H. Stoll, K. W. Chou, T. Tyliszczak, R. Hertel, M. Fahnle, H. Bruckl, K. Rott, G. Reiss, I. Neudecker, D. Weiss, C. H. Back, and G. Schutz, Nature (London) **444**, 461 (2006).

[2] K. Yamada, S. Kasai, Y. Nakatani, K. Kobayashi, H. Kohno, A. Thiaville, and T. Ono, Nat. Mater. **6**, 270 (2007).

[3] S. Wintz, V. Tiberkevich, M. Weigand, J. Raabe, J. Lindner, A. Erbe, A. Slavin, and J. Fassbender, Nat. Nanotechnol. **11**, 948 (2016).

[4] D. Reitz, A. Ghosh, and O. Tchernyshyov, Phys. Rev. B **97**, 054424 (2018).

[5] A. V. Bondarenko, E. Holmgren, Z. W. Li, B. A. Ivanov, and V. Korenivski, Phys. Rev. B **99**, 054402 (2019).

[6] A. Cuccoli, D. Nuzzi, R. Vaia, and P. Verrucchi, J. Magn. Magn. Mater. **400**, 149 (2016).

[7] M. S. Wolf, R. Badea, and J. Berezovsky, Nat. Commun. **7**, 11584 (2016).

[8] M. Noske, H. Stoll, M. Fähnle, R. Hertel, and G. Schütz, Phys. Rev. B **91**, 014414 (2015).

[9] R. Hertel and C. M. Schneider, Phys. Rev. Lett. **97**, 177202 (2006).

[10] A. Vansteenkiste, J. Leliaert, M. Dvornik, M. Helsen, F. Garcia-Sanchez, and B. Van Waeyenberge, AIP Adv. **4**, 107133 (2014).

[11] S. D. Sloetjes, E. Digernes, F. K. Olsen, R. V. Chopdekar, S. T. Retterer, E. Folven, and J. K. Grepstad, Appl. Phys. Lett. **112**, 042401 (2018).

[12] O. Tchernyshyov and G.-W. Chern, Phys. Rev. Lett. **95**, 197204 (2005).

[13] H. van den Berg and D. Vatvani, J. Appl. Phys. **52**, 6830 (1981).

[14] H. van den Berg and D. Vatvani, IEEE Trans. Magn. **18**, 880 (1982).

[15] A. Hubert and R. Schäfer, *Magnetic Domains: The Analysis of Magnetic Microstructures* (Springer Science & Business Media, Berlin, 2008).

[16] A. DeSimone, R. V. Kohn, S. Müller, F. Otto, and R. Schäfer, J. Magn. Magn. Mater. **242-245**, 1047 (2002).

[17] T. Nagai, H. Yamada, M. Konoto, T. Arima, M. Kawasaki, K. Kimoto, Y. Matsui, and Y. Tokura, Phys. Rev. B **78**, 180414(R) (2008).

[18] E. J. Kim, J. L. Watts, B. Harteneck, A. Scholl, A. Young, A. Doran, and Y. Suzuki, J. Appl. Phys. **109**, 07D712 (2011) .

[19] Y. Takamura, E. Folven, J. B. R. Shu, K. R. Lukes, B. Li, A. Scholl, A. T. Young, S. T. Retterer, T. Tybell, and J. K. Grepstad, Phys. Rev. Lett. **111**, 107201 (2013).

[20] D. L. Huber, Phys. Rev. B **26**, 3758 (1982).

[21] A. A. Thiele, Phys. Rev. Lett. **30**, 230 (1973).

[22] K. Y. Guslienko, K.-S. Lee, and S.-K. Kim, Phys. Rev. Lett. **100**, 027203 (2008).

[23] See Supplemental Material at http://link.aps.org/supplemental/10.1103/PhysRevB.101.014450 for movies showing the exchange explosions discussed in this paper.

[24] V. Estévez and L. Laurson, Phys. Rev. B **93**, 064403 (2016).

[25] N. L. Schryer and L. R. Walker, J. Appl. Phys. **45**, 5406 (1974).

[26] X. S. Wang, P. Yan, Y. H. Shen, G. E. W. Bauer, and X. R. Wang, Phys. Rev. Lett. **109**, 167209 (2012).

[27] V. Estévez and L. Laurson, Phys. Rev. B **91**, 054407 (2015).

[28] V. Estévez and L. Laurson, Phys. Rev. B **96**, 064420 (2017).

[29] X.-P. Ma, S.-D. Kim, S.-Y. Park, Y.S. Choi, H.-G. Piao, and D.-H. Kim, J. Appl. Phys. **124**, 083905 (2018).

[30] M.-Y. Im, H.-S. Han, M.-S. Jung, Y.-S. Yu, S. Lee, S. Yoon, W. Chao, P. Fischer, J.-I. Hong, and K.-S. Lee, Nat. Commun. **10**, 593 (2019).